Fluid permeabilities of triply periodic minimal surfaces

Y. Jung[1,2] and S. Torquato[1,2,3,*]
[1]*Princeton Institute for the Science and Technology of Materials, Princeton University, Princeton, New Jersey 08544, USA*
[2]*Department of Chemistry, Princeton University, Princeton, New Jersey 08544, USA*
[3]*Program in Applied and Computational Mathematics, Princeton University, Princeton, New Jersey 08544, USA*
(Received 15 June 2005; published 17 November 2005)

It has recently been shown that triply periodic two-phase bicontinuous composites with interfaces that are the Schwartz primitive (P) and diamond (D) minimal surfaces are not only geometrically extremal but extremal for simultaneous transport of heat and electricity. The multifunctionality of such two-phase systems has been further established by demonstrating that they are also extremal when a competition is set up between the effective bulk modulus and electrical (or thermal) conductivity of the bicontinuous composite. Here we compute the fluid permeabilities of these and other triply periodic bicontinuous structures at a porosity $\phi=1/2$ using the immersed-boundary finite-volume method. The other triply periodic porous media that we study include the Schoen gyroid (G) minimal surface, two different pore-channel models, and an array of spherical obstacles arranged on the sites of a simple cubic lattice. We find that the Schwartz P porous medium has the largest fluid permeability among all of the six triply periodic porous media considered in this paper. The fluid permeabilities are shown to be inversely proportional to the corresponding specific surfaces for these structures. This leads to the conjecture that the maximal fluid permeability for a triply periodic porous medium with a simply connected pore space at a porosity $\phi=1/2$ is achieved by the structure that globally minimizes the specific surface.

DOI: 10.1103/PhysRevE.72.056319 PACS number(s): 47.55.Mh, 05.60.Cd, 87.16.Dg

I. INTRODUCTION

Triply periodic minimal surfaces are objects of great interest to physical scientists, biologists, and mathematicians. A minimal surface, such as a soap film, is one that is locally area minimizing. Minimal surfaces are defined as surfaces with zero mean curvature. A remarkable class of minimal surfaces are those that are triply periodic (i.e., periodic in three directions). A triply periodic minimal surface is infinitely extending, has one of the crystallographic space groups as its symmetry group and, if it has no self-intersections, it partitions space into two disjoint but intertwining regions that are simultaneously continuous [1]. If one thinks of each of these disjoint regions as the phase of a composite, then those two-phase composites in which the interface is a triply periodic minimal surface are a special class of bicontinuous two-phase composites. The Schwartz primitive (P), the Schwartz diamond (D), and the Schoen gyroid (G) minimal surfaces partition space into two disjoint but congruent regions, i.e., the volume fraction of each phase is 1/2 (see Fig. 1). Triply periodic minimal surfaces arise in a variety of systems, including block copolymers [2], nanocomposites [3], micellar materials [4], lipid-water systems, and certain cell membranes [5–8].

It has been recently shown that triply periodic two-phase bicontinuous composites with interfaces that are the Schwartz P and D minimal surfaces are not only geometrically extremal, but are also extremal for simultaneous transport of heat and electricity [9,10]. More precisely, these are the optimal structures when a weighted sum of the effective thermal and electrical conductivities is maximized for the case in which phase 1 is a good thermal conductor but a poor electrical conductor and phase 2 is a poor thermal conductor but a good electrical conductor. The demand that this sum is maximized sets up a *competition* between the two effective transport properties, and this demand is met by the Schwartz P and D structures. We note that for reasons of mathematical analogy, the optimality of these bicontinuous composites applies to any of the pair of the following scalar effective properties: electrical conductivity, thermal conductivity, dielectric constant, magnetic permeability, and diffusion coefficient.

Since triply periodic minimal surfaces arise in certain cell membranes, it stands to reason that such structures must also be relatively stiff elastically in order to withstand mechanical loads. The topological property of bicontinuity of these structures suggests that they would be mechanically stiff even if one of the phases is a compliant solid or a liquid, provided that the other phase is a relatively stiff material. Motivated by this biological example, Torquato and Donev [11] asked what are the two-phase composite structures that maximize a weighted sum of the dimensionless effective bulk modulus and effective electrical (or thermal) conductivity. Thus, they set up a competition between a mechanical property and a transport property. They demonstrated that triply periodic two-phase bicontinuous composites with interfaces that are the Schwartz P and D minimal surfaces are again optimal, further establishing the multifunctionality of such two-phase systems.

Based on the aforementioned considerations, it is reasonable to inquire whether the minimal surfaces are optimal for other effective properties, such as flow characteristics. The purpose of this paper is to study Stokes (slow viscous) flow through triply porous media whose interfaces are the Schwartz P, the Schwartz D, and the Schoen G minimal surfaces. In particular, we are interested in computing the fluid

*Corresponding author. Electronic address: torquato@electron.princeton.edu

permeability k, which is the key macroscopic property for describing Stokes flow through porous media [12–15]. The quantity k is the proportionality constant between the average fluid velocity and applied pressure gradient in the porous medium as defined by Darcy's law:

$$\bar{U} = -\frac{k}{\mu}\nabla p, \tag{1}$$

where $\bar{U}$ is the average fluid velocity, ∇p is the applied pressure gradient, and μ is the dynamic viscosity. Our expectation is that the Schwartz P porous medium will have the highest fluid permeability among the three minimal surfaces because it has the smallest *specific surface* (i.e., interface area per unit volume). The surface area alone, of course, does not necessarily inversely correlate with fluid permeability [12,14]. We will show that the Schwartz P porous medium does indeed have the highest fluid permeability among the three minimal surfaces. A natural question to ask is whether the fluid permeability of the Schwartz P porous medium is maximal in any sense. Although we do not answer this challenging question here, we also compute fluid permeabilities for other triply periodic geometries, such as flow over spheres arranged on the sites of a simple lattice and flow inside two different pore-channel models at a porosity (volume fraction of pore space) $\phi = 1/2$. We find that the Schwartz P porous medium has the highest fluid permeability among all of the six triply periodic porous media considered in this paper. We demonstrate that the fluid permeabilities are inversely proportional to the corresponding specific surfaces for these structures. This leads to the reasonable conjecture that the maximal fluid permeability (scaled by the cell length squared) for a triply periodic porous medium with a simply connected pore space at a porosity $\phi = 1/2$ is achieved by the structure that globally minimizes the specific surface.

Due to the numerical difficulties in generating complex meshes of various minimal surfaces, the immersed-boundary finite-volume method was adopted in this paper [16,17]. Momentum forcing is applied on the body surface or inside the body to satisfy the no-slip boundary condition on the immersed boundary and to satisfy the continuity for the each control volume element containing the immersed body. This procedure is based on a finite-volume approach on a staggered mesh with a fractional step method. The unit domain is chosen to be a cube and is digitized into small cubic subvolumes.

In Sec. II, we review some procedures to represent triply periodic minimal surfaces. In Sec. III, the immersed-boundary finite-volume method for flow through triply periodic porous media is described. In Sec. IV, we verify the accuracy of our numerical methods by computing the fluid permeability for the flow over spheres arranged on the sites of a simple cubic and compare them to corresponding analytical/numerical results of Sangani and Acrivos [18]. Here we also present our evaluations of the fluid permeabilities for other triply periodic porous media, including Schwartz P and D surfaces, the Schoen G surface, and two different pore-channel models. Concluding remarks and a discussion are given in Sec. V.

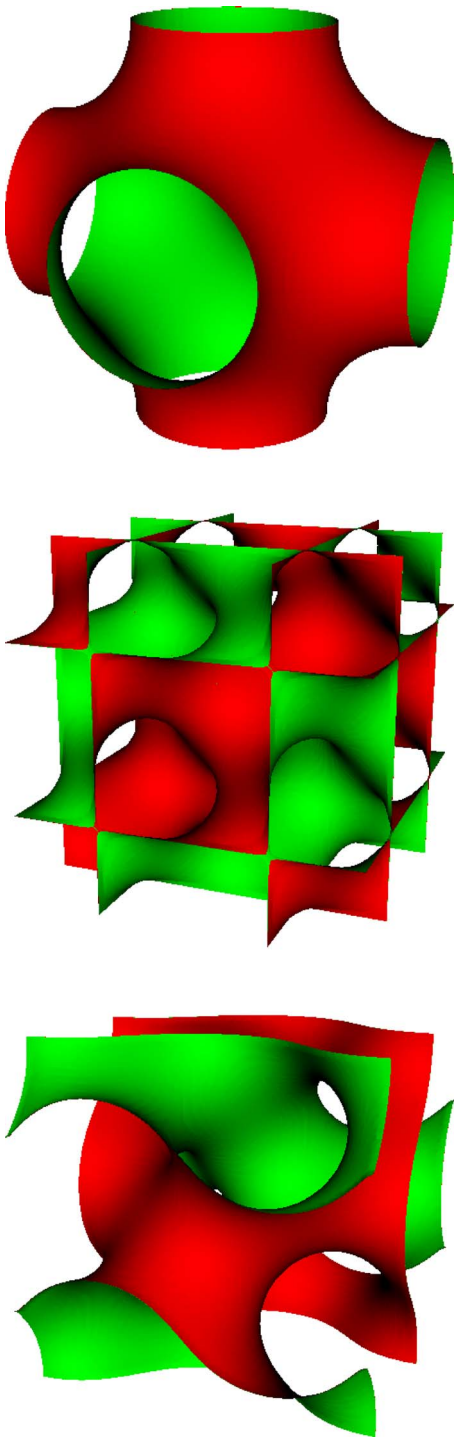

FIG. 1. (Color online) Unit cells of three different minimal surfaces. Top panel: Schwartz primitive (P) surface. Center panel: Schwartz diamond (D) surface. Bottom panel: Schoen gyroid (G) surface.

II. TRIPLY PERIODIC MINIMAL SURFACES

Triply periodic minimal surfaces can be characterized exactly using an Enneper-Weierstrass (complex integration) representation only for several cases. For Schwartz P and D and Schoen G, analytic surfaces are constructed in terms of elliptic functions by the Enneper-Weierstrass representation

[19–21], but in practice this is difficult to use numerically. Recently, it was shown that triply periodic minimal surfaces can be generated as the local minima of the scalar order parameter Landau-Ginzburg functional for describing ordering phenomena in microemulsion [22]. This Landau-Ginzburg free-energy functional [22] can be utilized to calculate numerically a discretization of a potential $\psi(x)$ such that $\psi(x)>0$ for points in phase 1 and $\psi(x)<0$ for points in phase 2. At the phase interface, $\psi(x)=0$, which in this case is a Schwartz P, D, or Schoen G minimal surface. Moreover, the minimal surfaces can be approximated by the periodic nodal surface (PNS) of a sum defined in terms of the Fourier series [23–26], because any periodic surface can be expressed as the sum of an infinite number Fourier terms.

In this paper, the Schwartz P and D and the Schoen G surfaces are produced by both the Landau-Ginzburg minimization [22] and PNS approximations with a few Fourier terms [25,26] on a 129^3 unit cell. From these potentials, one can readily make discretizations of triply periodic bicontinuous two-phase composites in which the two-phase interface is a minimal surface. Because phase 1 is topologically and geometrically identical to phase 2, either phase can be chosen to be the fluid phase. Indeed, triply periodic minimal surfaces have the special property that the fluid permeability of phase 1 is equal to the fluid permeability of phase 2. Such phase interchange relations are rare in the case of the fluid permeability. By contrast, phase interchange relations in the case of the effective conductivity and effective elastic moduli of two-phase composites have been known for a long time; see [14,27,28] and references therein. We used an immersed-boundary finite-volume method (described below) to calculate numerically the fluid permeabilities of these composites.

III. NUMERICAL SIMULATION FOR STOKES FLOW THROUGH TRIPLY PERIODIC POROUS MEDIA

We consider the flow field in an infinite porous medium. The Navier-Stokes equations are nondimensionalized with; $t' := \mu t/(\rho L^2)$ and $p' := (p-p_0)/(\mu U/L)$, where t is the time, μ is the dynamic viscosity, ρ is the density, L is the characteristic length, p is the pressure, p_0 is the pressure at a reference, and U is the characteristic speed. Dropping the primes leads to the dimensionless Navier-Stokes equations

$$\frac{\partial u_i}{\partial t} + \mathrm{Re}\left(\frac{\partial u_i u_j}{\partial x_j}\right) = -\frac{\partial p}{\partial x_i} + \frac{\partial}{\partial x_j}\frac{\partial u_i}{\partial x_j},$$
$$\frac{\partial u_i}{\partial x_i} = 0, \tag{2}$$

where t is the dimensionless time, x_j's are the dimensionless Cartesian coordinates ($j=1$, 2, or 3), u_i's are the corresponding dimensionless velocity components, p is the dimensionless pressure, and $\mathrm{Re}=\rho UL/\mu$ is the Reynolds number [29].

In the limit $\mathrm{Re}\to 0$, we obtain the dimensionless unsteady Stokes flow equations, which is of central concern in this study. These unsteady Stokes equations recover the steady Stokes formulation for the infinite time advancement. Due to the numerical difficulties in generating complex meshes of various minimal surfaces, the immersed-boundary finite-volume method was adopted in this paper [16,17]. The discrete-time momentum forcing, f_i, is applied to satisfy the no-slip condition on the immersed boundary. The forcing points are located in a staggered fashion, like the velocity components defined on a staggered grid (see Fig. 2). Therefore, the governing equations for unsteady incompressible stokes flow becomes

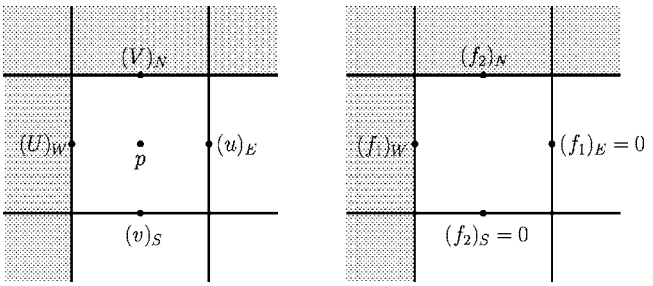

FIG. 2. Forcing points in staggered mesh.

$$\frac{\partial u_i}{\partial t} = -\frac{\partial p}{\partial x_i} + \frac{\partial}{\partial x_j}\frac{\partial u_i}{\partial x_j} + f_i,$$
$$\frac{\partial u_i}{\partial x_i} = 0, \tag{3}$$

where f_i's are the dimensionless momentum forcing components defined at the cell faces on the immersed boundary and inside the body.

The Stokes equations represented by Eq. (3) are advanced with a fully implicit, fractional step method [16,30] with the Crank-Nicholson method in convection term. The fractional step, or time-split method, approximates the evolution equation by decomposition of the operators in it. A four-step time advancement [31] is modified for time integration of Eq. (3) as follows:

$$\frac{\hat{u}_i - u_i^n}{\Delta t} = -\frac{\partial p^n}{\partial x_i} + \frac{1}{2}\frac{\partial}{\partial x_j}\frac{\partial}{\partial x_j}(\hat{u}_i + u_i^n) + f_i^n, \tag{4}$$

$$\frac{\bar{u}_i - \hat{u}_i}{\Delta t} = \frac{\partial p^n}{\partial x_i}, \tag{5}$$

$$\frac{\partial}{\partial x_i}\frac{\partial p^{n+1}}{\partial x_i} = \frac{1}{\Delta t}\frac{\partial \bar{u}_i}{\partial x_i}, \tag{6}$$

$$\frac{u_i^{n+1} - \bar{u}_i}{\Delta t} = -\frac{\partial p^{n+1}}{\partial x_i}. \tag{7}$$

Here, the solution u_i^n at time step, n is advanced to u_i^{n+1} at time step $n+1$ through intermediate velocities $\hat{u}_i$ and $\bar{u}_i$. explicit direct-forcing scheme for the momentum equation is utilized to obtain the momentum forcing value in Eq. (4), which should be known *a priori* for time advancement [32]. Discretizing Eq. (4) explicitly in time and rearranging it for f_i^n at a forcing point results in

$$f_i^n = \frac{\hat{U}_i - u_i^n}{\Delta t} + \frac{\partial p^n}{\partial x_i} - \frac{\partial}{\partial x_j}\frac{\partial u_i^n}{\partial x_j}, \tag{8}$$

where $\hat{U}_i$ is the velocity imposed at a forcing point to enforce $u_i^n = \hat{U}_i$ on the immersed boundary. To satisfy the no-slip boundary condition on the immersed boundary, $\hat{U}_i$ is zero when the forcing point is at the immersed boundary or inside the body. All the spatial derivatives are resolved with the second-order central-difference scheme using a staggered mesh system. The discretized momentum equations are factorized into three operators, which require inversion of tridiagonal matrices. Time advancement is achieved by sweeping x_1-, x_2-, and x_3-direction tridiagonal matrix algorithm at time intervals of $n+\frac{1}{3}$, $n+\frac{2}{3}$, and $n+1$.

To drive flow in a unit cell of a triply periodic porous medium, a pressure drop is applied from the inlet to the outlet of the channel in one of the three directions (x_1 in this paper). In the other two directions (x_2 and x_3), standard treatment for velocity and pressure periodic boundary conditions are applied. To solve the elliptic pressure Eq. (6), the alternating direction implicit (ADI) method is applied with a relaxation. Nonuniqueness of a pressure solution due to applying a pressure drop condition can be resolved with a point constraint which imposes an arbitrary pressure value at an arbitrary position. In fact, the pressure gradient only is necessary for solving the velocity field. When the triply periodic surface possesses simple cubic symmetry, the periodic boundary conditions can be exploited further. Because of the mirror image of the flow and pressure field across $x_2=0.5$ and $x_3=0.5$ in the unit size channel simulation, the simple cubic symmetry motivates setting the velocity and pressure at the reflection position across the middle cross section.

In general, the forcing point of an arbitrary immersed body does not coincide with the immersed boundary, but rather inside the body in the nonbody-fitted Cartesian mesh. This requires a velocity interpolation to impose the correct $\hat{U}_i$ at a forcing point. However, no velocity interpolation scheme is necessary to satisfy the no-slip boundary condition on the immersed boundary in this paper because in the digitized triply periodic surfaces, the forcing point of an immersed body always coincides with the immersed boundary.

IV. NUMERICAL RESULTS

In this section, we will apply the immersed-boundary method to determine the Stokes flow velocity fields in triply periodic porous media with cubic symmetry. We begin by computing the flow field for a periodic array of spheres in order to validate the procedure and the numerical results. Subsequently, we apply the numerical procedure to two different pore-channel models as well as the bicontinuous structures with interfaces that are the Schwartz P and D minimal surfaces, and the Schoen G minimal surfaces. The permeability results for all six cases are compared at the porosity $\phi = 1/2$. The fluid permeabilities are obtained from the imposed pressure drop Δp and average velocity $\bar{U}$ of the flow field in the cubic periodic cell of the side length L. Because of the cubic symmetry, the second-order fluid permeability tensor is isotropic (i.e., it is given by $k\mathbf{I}$, where $\mathbf{I}$ is the identity tensor) [14], and therefore the determination of the permeability along the x_1 axis is sufficient to characterize k. From Eq. (1), the fluid permeability k can be made dimensionless by dividing it by L^2. Henceforth, all permeabilities will be reported in this dimensionless form.

TABLE I. The fluid permeability k for Stokes flow past simple cubic lattices of spheres. Here $\chi=(c/c_{max})^{1/3}$, where c is the particle volume fraction and $c_{max}=\pi/6$.

χ	k (Present work)	k (Sangani and Acrivos[a])
0.1	9.1467×10^{-1}	9.1107×10^{-1}
0.2	3.8436×10^{-1}	3.8219×10^{-1}
0.3	2.1069×10^{-1}	2.0805×10^{-1}
0.4	1.2516×10^{-1}	1.2327×10^{-1}
0.5	7.6379×10^{-2}	7.4668×10^{-2}
0.6	4.5803×10^{-2}	4.4501×10^{-2}
0.7	2.6059×10^{-2}	2.5246×10^{-2}
0.8	1.3758×10^{-2}	1.3197×10^{-2}
0.85	9.5964×10^{-3}	9.1516×10^{-3}
0.9	6.4803×10^{-3}	6.1531×10^{-3}
0.95	4.2473×10^{-3}	4.0031×10^{-3}
1.0	2.6727×10^{-3}	2.5203×10^{-3}

[a]Reference [18].

The computational domain is chosen to be a unit cube and staggered Cartesian meshes were generated, depending on the required resolution. All initial velocities and pressures are set equal to zero.

A. Periodic array of spheres

To verify the numerical accuracy of the immersed-boundary method, we compare our calculations to the analytical/numerical results of Sangani and Acrivos [18] for flow past periodic arrays of spheres centered on the sites of a

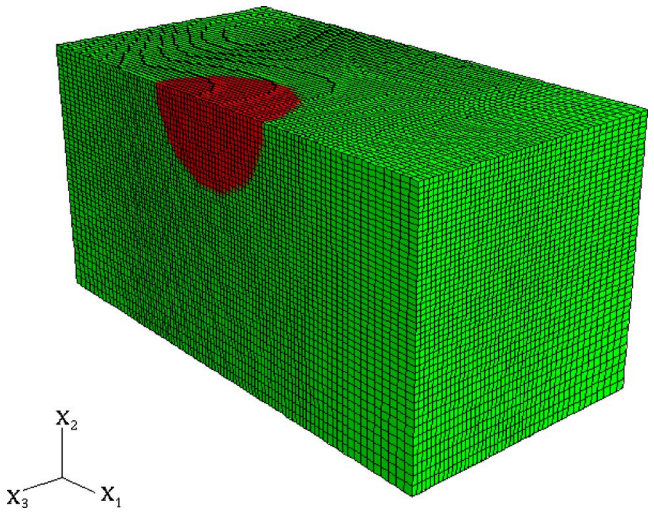

FIG. 3. (Color online) Mesh for a flow field over a sphere.

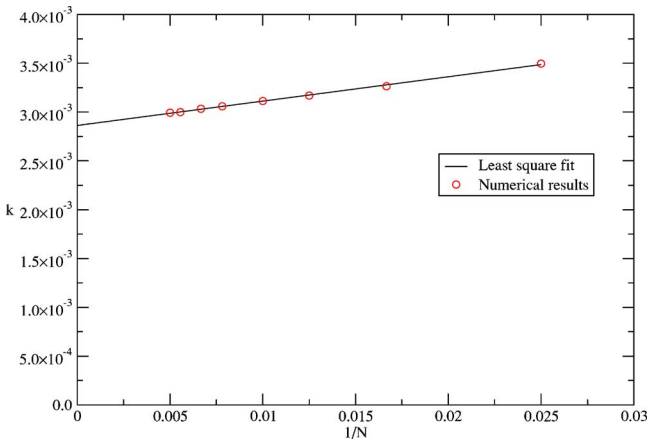

FIG. 4. (Color online) Fluid permeability k for Stokes flow past a simple cubic array of equisized spherical obstacles as a function of $1/N$ for $\phi=1/2$.

simple cubic lattice. The immersed body (sphere in this case) is constructed using the following criterion. The immersed sphere is identified if the center of each voxel constituting a single sphere centered at (0.5, 0.5, 0.5) satisfies the equation

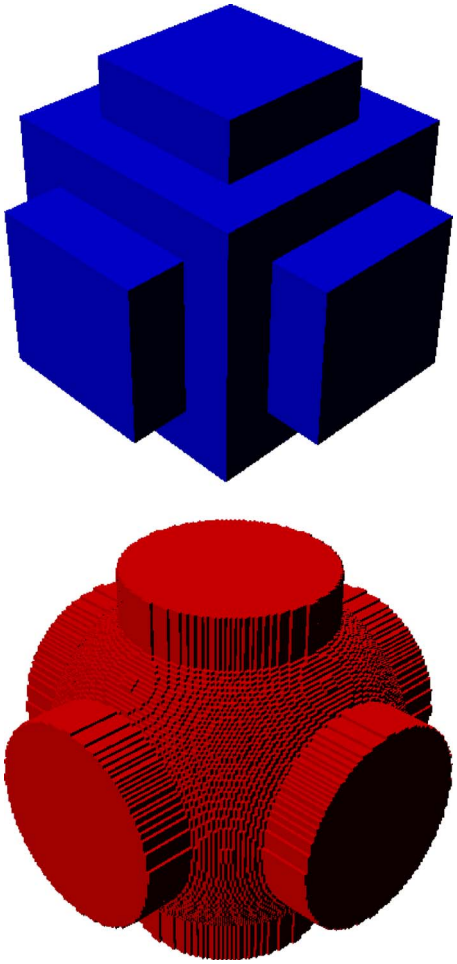

FIG. 5. (Color online) Unit cells of two different pore-channel models. Top panel: cubic pore-square channel. Bottom panel: spherical pore-circular channel.

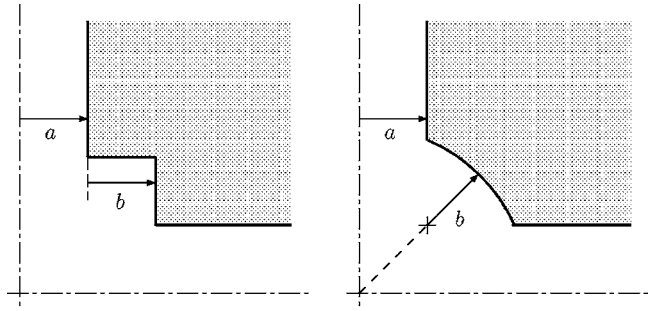

FIG. 6. Cross sections of the two different pore-channel models.

$$(x_1-0.5)^2+(x_2-0.5)^2+(x_3-0.5)^2 \leqslant r^2, \qquad (9)$$

where r is the radius of the sphere. As explained in Sec. III, a pressure drop is applied in the x_1 direction, and standard treatment for velocity periodic boundary conditions are applied in x_2 and x_3 directions. The fluid permeability k obtained from numerical simulations are listed in Table I for various values of the scaled particle volume fraction $\chi=(c/c_{max})^{1/3}$, where c is the particle volume fraction, and $c_{max}=\pi/6$ is the maximum particle volume fraction corresponding to the case when the spheres are in contact. Our fluid permeability calculations are in good agreement with the results of Sangani and Acrivos [18].

Nonuniform (stretching) staggered meshing is used toward the body over the computational domain to get the required spatial accuracy for the immersed-boundary method, which is important for the comparison of our permeability data to corresponding analytical/numerical results over a smooth sphere (see Fig. 3). The discretization of a continuous body with a finite resolution obviously affects the numerical accuracy of the computed fluid permeability k, which depends on the value of the grid mesh spacing h or the mesh resolution $N=1/h$. We studied the resolution effects on the numerical accuracy at fixed porosity $\phi=1/2$. The fluid permeability data and a corresponding linear least-squares fit are shown against $1/N$ in Fig. 4.

TABLE II. The fluid permeability for the cubic pore-square channel model for several porosites and geometric parameters a and b.

ϕ	a	b	k
0.5	0.2500	0.0000	3.0744×10^{-3}
	0.1324	0.2500	0.5310×10^{-3}
	0.0781	0.3125	0.0948×10^{-3}
0.7	0.3125	0.0000	9.1168×10^{-3}
	0.2656	0.1406	6.2495×10^{-3}
	0.2250	0.2000	3.7939×10^{-3}
0.9	0.4000	0.0000	26.207×10^{-3}
	0.3750	0.0750	23.915×10^{-3}
	0.2625	0.2125	8.0231×10^{-3}

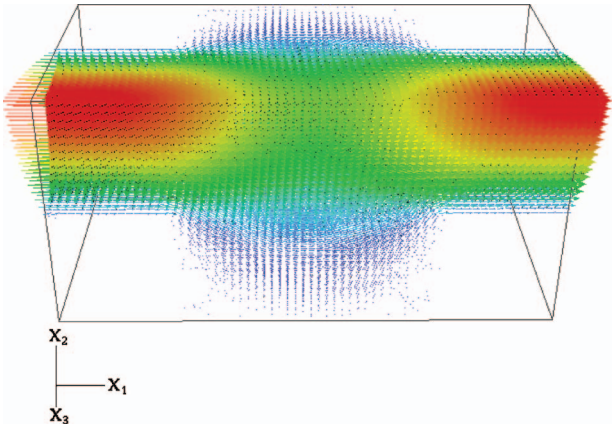

FIG. 7. (Color) The flow field in a unit cell of the triply periodic cubic pore-square channel geometry for the minimal pore case ($a=0.250$, $b=0$) at porosity $\phi=1/2$. Color scheme: red, yellow, green, light blue, and blue represent the spectrum of speeds from highest to lowest, respectively.

Various mesh resolutions ($N=20$, 40, 60, 80, 128, 150, 180, 200) are used to reduce the digitization error over solid regions in these simulations. Generally, fluid permeabilities determined from the immersed-boundary method for digitized spheres are overestimated but this error, as Table I shows, decreases as the resolution increases.

B. Bicontinuous triply periodic porous media

Before describing our results for the minimal surfaces, we first consider two different pore-channel models that are also bicontinuous and triply periodic. The latter is motivated by the fact that one-dimensional flows inside channels are characterized by high permeabilities. However, since we are interested in macroscopically isotropic permeabilities (i.e., cases when the fluid permeability tensor is isotropic), we consider triply periodic channels that intersect in three orthogonal directions (x_1, x_2, and x_3). A pore in this model is the region where the channels meet and its geometry depends on the geometry of the channel. In one model, we consider square channels and cubic pores. In the second model, we consider circular channels and spherical pores (see Fig. 5).

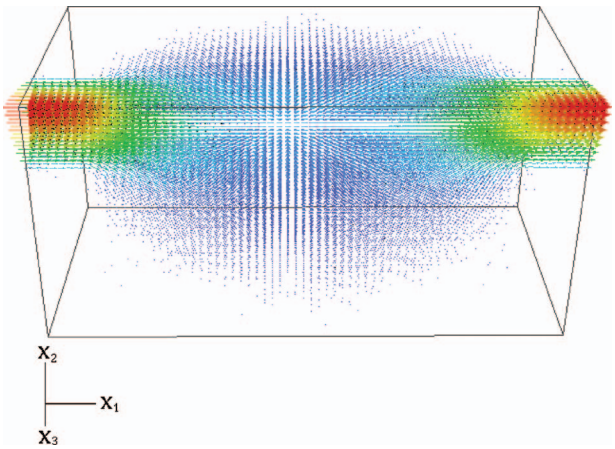

FIG. 8. (Color) The flow field in a unit cell of the triply periodic cubic pore-square channel geometry for the case $a=0.132$, $b=0.250$ at porosity $\phi=1/2$. The color scheme for speeds is the same as described in Fig. 7.

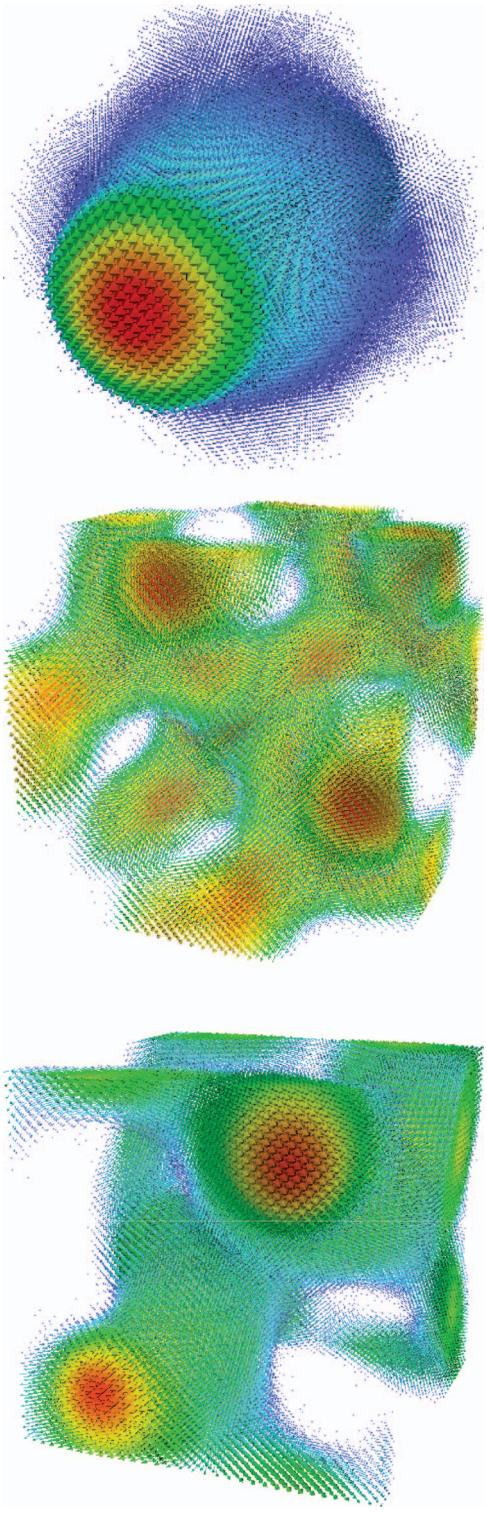

FIG. 9. (Color) Flow fields for triply periodic porous media with interfaces that are minimal surfaces. Top panel: Schwartz P surface. Center panel: Schwartz D surface. Bottom panel: Schoen G surface. The color scheme for speeds is the same as described in Fig. 7.

Cross sections of the two models are shown in Fig. 6, where a and b are the parameters that enable us to control the relative pore-channel geometries. For example, in the case of the cubic pore-square channel or spherical pore-circular channel, the pore is defined to be *minimal* when $b=0$.

1. Pore-channel models

We calculated the permeability k for three different combinations of a and b at three porosities $\phi=0.5$, 0.7 and 0.9 on fine mesh of $128\times128\times128$. Table II summarizes our permeability results for the cubic pore-square channel geometry. Not surprisingly, the permeability increases with increasing porosity ϕ. The minimal pore case (i.e., $b=0$) provided the highest permeability at any porosity. As shown in Fig. 7, channel flow away from the channel intersection (both upstream and downstream) has a Poiseuille-type flow profile but, in the vicinity of the channel intersection, the flow is no longer confined and the associated maximum speed in the x_2-x_3 plane is reduced. This is illustrated in Fig. 7, where the speed profile is for the minimal pore case. Increasing the pore size while keeping the porosity fixed, leads to an even lower maximum speed, as depicted in Fig. 8. Consequently, the pore region at the channel intersection has a significant effect on the overall flow field and hence fluid permeability of the porous media.

We also computed fluid permeabilities for the spherical pore-circular channel geometry, but since the trends are the same as in Table II, we do not present all of these results here. In the minimal pore case ($b=0$), the fluid permeability of the circular channel geometry ($k=3.4596\times10^{-3}$) is larger than the corresponding square channel case ($k=3.0743\times10^{-3}$). Moreover, the circular channel has a lower specific surface than the square channel at the same porosity. This point will be discussed further below.

2. Triply periodic minimal surfaces

Here we report results for the fluid permeability of triply periodic porous media with interfaces that are the Schwartz P and D surfaces, and the Schoen G surface. The minimal surfaces are generated from the aforementioned Landau-Ginzburg potential minimization and each has a fine mesh resolution of $129\times129\times129$. The potential data $\psi(x)$ are numerically digitized such that $\psi(x)>0$ for points in phase 1 and $\psi(x)<0$ for points in phase 2 or vice versa.

It is found that the computational difficulty due to the geometrical complexities are very well treated by the immersed-boundary finite-volume method. Representative flow fields over the minimal surfaces are shown in Fig. 9. Our computed fluid permeabilities for the three minimal surfaces are summarized in Table III, along with corresponding results for the circular and square channels with minimal pores, and the simple cubic array of spherical obstacles at the porosity $\phi=1/2$. It should be noted that the Schwartz P surface has the highest fluid permeability among these six triply periodic porous media. Included in the table is the specific surface s for each of the structures. The fluid permeabilities are seen to be inversely proportional to the specific surfaces. Thus, the Schwartz P surface has the largest fluid permeability followed by the circular channel, square channel, spherical obstacle, and finally the Schoen G and the Schwartz D surface cases. The permeability of the circular channel with a minimal pore is actually close in value to that of the Schwartz P surface. Evidently, the sharp corner present in the former results in slightly greater energy dissipation than in the smooth Schwartz P surface.

TABLE III. The fluid permeability k and the specific surface s at $\phi=1/2$ for six different triply periodic porous media models. The pore-channel results are presented for the minimal pore case ($b=0$). SC and BCC stand for simple cubic and body centered cubic lattices, respectively.

Model	k	s	Symmetry
Schwartz P surface	3.4765×10^{-3}	2.3705	SC
Spherical pore-circular channel	3.4596×10^{-3}	2.6399	SC
Cubic pore-square channel	3.0743×10^{-3}	3.0000	SC
Spherical obstacle	3.0591×10^{-3}	3.0780	SC
Schoen G surface	2.2889×10^{-3}	3.1284	BCC
Schwartz D surface	1.4397×10^{-3}	3.9011	SC

V. CONCLUSIONS AND DISCUSSION

We have determined the Stokes flow fields and associated fluid permeabilities through six different triply porous media: the Schwartz P, the Schwartz D, and the Schoen G minimal surfaces, two different pore-channel models, and a simple cubic array of spherical obstacles. The latter model served as a benchmark to verify the accuracy of our numerical procedure: the immersed-boundary finite-volume method. We found good agreement with previous results for the simple cubic array. Interestingly, we found that the Schwartz P porous medium has the highest fluid permeability among all of the six triply periodic porous media considered in this paper. The fluid permeabilities were shown to be inversely proportional to the specific surfaces for these bicontinuous structures. This might lead one to conjecture that the maximal fluid permeability (scaled by the cell length squared) for a triply periodic porous medium at a porosity $\phi=1/2$ is achieved by the structure that globally minimizes the specific surface. As we pointed out in the Introduction, the specific surface does not necessarily correlate with the permeability. However, the pore spaces of structures with large permeabilities are expected to be *simply connected* and therefore it would not be unreasonable for the permeability to be inversely proportional to the specific surface in these instances.

The determination of the structure that globally optimizes the fluid permeability is a highly challenging problem. It is only recently that optimal bounds on k have been identified. By contrast, optimal bounds on the effective conductivity and elastic moduli of two-phase composite media have long been known [14,28]. In particular, Torquato and Pham [33] showed that the so-called void upper bounds on k for flow in anisotropic media with a single preferred direction are opti-

mal for certain coated-cylinders models. Such structures arise in practice in sea ice, for example, which has a microstructure that is well modeled by oriented cylindrical channels [34]. However, these bounds are not applicable for our present purposes because we would like to ascertain the triply periodic structure that maximizes the isotropic permeability. Even if the conjecture that the maximal dimensionless fluid permeability for a triply periodic porous medium with a simply connected pore space at a porosity $\phi=1/2$ is achieved by the structure that globally minimizes the specific surface is true, finding the minimizing specific surface structure is highly nontrivial. For example, Kelvin's problem, the determination of the space-filling arrangement of *closed* cells of equal volume that minimizes the surface area, is still an open question, although it is believed that the Weaire-Phelan structure [35] is a good candidate. In a future work, we will determine whether the Schwartz P triply periodic porous medium is a locally maximal structure for the isotropic fluid permeability.

ACKNOWLEDGMENTS

The authors are grateful to Volodymyr Babin and Wojciech Góźdź for providing TPMS data and to Jung-Il Choi for helpful discussions. This work was supported by the Air Force Office of Scientific Research under Grant No. F49620-03-1-0406.

[1] D. M. Anderson, H. T. Davis, L. E. Scriven, and J. C. C. Nitsche, Adv. Chem. Phys. **77**, 337 (1990).
[2] P. D. Olmstead and S. T. Milner, Macromolecules **31**, 4011 (1998).
[3] L. Yunfeng, Y. Yang, A. Sellinger, M. Lu, J. Huang, H. Fan, R. Haddad, G. Lopez, A. R. Burns, D. Y. Sasaki, J. Shelnutt, and C. J. Brinker, Nature (London) **410**, 913 (2001).
[4] P. Ziherl and R. D. Kamien, Phys. Rev. Lett. **85**, 3528 (2000).
[5] *Micelles, Membranes, Microemulsions, and Monolayers*, edited by W. M. Gelbart, A. Ben-Shaul, and D. Roux, (Springer Verlag, New York, 1994).
[6] T. Landh, FEBS Lett. **369**, 13 (1995).
[7] J. Klinowski, A. L. Mackay, and H. Terrones, Philos. Trans. R. Soc. London **354**, 1975 (1996).
[8] National Research Council, *Biomolecular Self-Assembling Materials: Scientific and Technological Frontiers* (National Academy Press, Washington, D.C., 1996).
[9] S. Torquato, S. Hyun, and A. Donev, Phys. Rev. Lett. **89**, 266601 (2002).
[10] S. Torquato, S. Hyun, and A. Donev, J. Appl. Phys. **94**, 5748 (2003).
[11] S. Torquato and A. Donev, Proc. R. Soc. London, Ser. A **460**, 1849 (2004).
[12] D. L. Johnson, J. Koplik, and L. M. Schwartz, Phys. Rev. Lett. **57**, 2564 (1986).
[13] S. Feng, B. I. Halperin, and P. N. Sen, Phys. Rev. B **35**, 197 (1987).
[14] S. Torquato, *Random Heterogeneous Materials: Microstructure and Macroscopic Properties* (Springer-Verlag, New York, 2002).
[15] M. Sahimi, *Heterogeneous Materials I: Linear Transport and Optical Properties* (Springer-Verlag, New York, 2003).
[16] J. Kim and P. Moin, J. Comput. Phys. **59**, 308 (1985).
[17] E. Fadlun, R. Verzicco, P. Orlandi, and J. Mohd-Yusof, J. Comput. Phys. **161**, 35 (2000).
[18] A. Sangani and A. Acrivos, Int. J. Multiphase Flow **8**, 343 (1982).
[19] P. Gandy, D. Cvijović, A. Mackay, and J. Klinowski, Chem. Phys. Lett. **314**, 543 (1999).
[20] P. Gandy and J. Klinowski, Chem. Phys. Lett. **321**, 363 (2000).
[21] P. Gandy and J. Klinowski, Chem. Phys. Lett. **322**, 579 (2000).
[22] W. T. Góźdź and R. Hołyst, Phys. Rev. E **54**, 5012 (1996).
[23] H. von Schnering and R. Nesper, Z. Phys. B: Condens. Matter **83**, 407 (1991).
[24] A. Mackay, Proc. R. Soc. London **A442**, 47 (1993).
[25] U. S. Schwarz and G. Gompper, Phys. Rev. E **59**, 5528 (1999).
[26] P. Gandy, S. Bardhan, A. L. Mackay, and J. Klinowski, Chem. Phys. Lett. **336**, 187 (2001).
[27] L. V. Gibiansky and S. Torquato, Int. J. Eng. Sci., **34**, 739 (1996).
[28] G. W. Milton, *The Theory of Composites* (Cambridge University Press, Cambridge, 2002).
[29] M. Deville, P. Fischer, and E. Mund, *High-Order Methods for Incompressible Fluid Flow* (Cambridge University Press, Cambridge, 2002).
[30] H. Le and P. Moin, J. Comput. Phys. **92**, 369 (1991).
[31] H. Choi and P. Moin, J. Comput. Phys. **113**, 1 (1994).
[32] J. Kim, D. Kim, and H. Choi, J. Comput. Phys. **171**, 132 (2001).
[33] S. Torquato and D. C. Pham, Phys. Rev. Lett. **92**, 255505 (2004); D. C. Pham and S. Torquato, J. Appl. Phys. **97**, 013535 (2005).
[34] K. Golden (unpublished).
[35] D. Weaire and R. Phelan, Philos. Mag. Lett. **69**, 107, 1994.